Features of the process of formation and dispersion of a liquid layer and formation of powder particles in plasma-arc atomization of current-conducting solid and flux-cored wires

Shiyi Gao[1], Ihor Kryvtsun[2], Volodymyr Korzhyk[1,2], Dmytro Strohonov[2*] ,
Oleksii Burlachenko[2], Oleksii Demianov[2], Oleksii Tereshchenko[2]

[1] China-Ukraine Institute of Welding, Guangdong Academy of Sciences, Guangdong Provincial Key Laboratory of Material Joining and Advanced Manufacturing: 363, Changxing Road, Tianhe, Guangzhou, 510650, China
[2] E.O. Paton Electric Welding Institute, National Academy of Sciences of Ukraine, 11 Kazymyr Malevych St., 03150 Kyiv, Ukraine
* Corresponding author's email: strogonovd94@gmail.com

ABSTRACT

The paper gives the results of mathematical modeling and experimental studies of the processes of formation and fragmentation of the liquid layer and formation of powder particles in plasma-arc atomization of current-conducting solid stainless steel AISI 316L wire and flux-cored Fe-Al wire. Mathematical modeling showed that initial fragments of size d_0 = 670–780 μm form at plasma-arc atomization of the above-mentioned wires, where after their separation from the tip of the atomized wire their multiple disintegration in the plasma jet takes place, which ends at the distance of ~ 120 mm with formation of fine spherical fragments (powders) with the average diameter of 105–125 μm. Experimental studies on determination of the initial size of the drops, forming at metal drop separation from the liquid layer, using high-speed filming, showed that their size is d_0 = 720–815 μm, and size of atomization products (powder) determined using the sieve analysis method are equal to 119–142 μm. Comparison of the obtained experimental and calculated data showed that that for atomization of both the solid stainless steel AISI 316L wire and flux-cored wire of Fe-Al system the main fraction of powder particles is 1–300 μm, which makes up 96–99 wt. % in both the cases, the error between the theoretical and experimental data being not higher than 7–32 %, depending on powder fraction, allowing application of the mentioned mathematical complex model to determine the optimal modes of plasma-arc atomization process with a wide range of wire materials. The study of the shape parameters and structure of AISI 316L and Fe-Al powders showed that most of the particles have a regular spherical shape with a sphericity coefficient close to 0.8–0.9, the microstructure of which is characterized by the absence of pores and voids.

Keywords: numerical modeling, plasma-arc atomization, melt fragmentation, current-conducting solid wires, flux-cored wires, spherical powders.

INTRODUCTION

Recently, due to the intensive development of the aviation, rocketry, space, medical, energy, and chemical industries, there is a need for complex shapes parts production of titanium alloys, nickel superalloys, refractory metals, intermetallics, mainly using additive technologies [1, 2].

The main additive technologies include: selective laser melting and sintering (SLM – selective laser melting, SLS – selective laser sintering), electron beam melting (EBM electron beam melting), direct laser (LDED – laser direct energy deposition) and plasma deposition (PMD – plasma metal deposition), cold spraying deposition (CSAM – cold spraying additive manufacturing) methods. All of these methods use specialized spherical powders (mostly fine) as consumables for the formation of additive layers with strict requirements for particle size

distribution, shape, physical, chemical and technological properties. For example, for the SLM, CS processes, powders of a narrow fraction of 15–45 μm, EBM 45–106 μm, for LDED 45–150 μm, and for PMD technology fractions of 63–160 μm are used [3–5]. In addition, these powders should have a spherical shape with a minimum number of external (satellites) and internal defects (pores, voids), good technological properties (high flowability, bulk density, sphericity coefficient, etc.) and a low content of gas inclusions, which ensures high packing density of additive layers, reduced porosity, and improved mechanical properties of the final product [6–8].

Currently, the most common technology for obtaining spherical powders for additive manufacturing is gas atomization (GA) which includes two main methods – VIGA (vacuum inert gas atomization) and EIGA (Electrode Induction Melting Inert Gas Atomization). Despite a number of advantages described in [9, 10], this technology has a number of significant disadvantages, namely [10–13]:

- the presence of a significant number of satellites and irregularly shaped particles, a lower sphericity coefficient for melt gas atomization methods, which causes poor flowability and bulk density (especially for a fine fraction < 63 μm) and leads to the formation of defects in the deposited layers;
- the presence of intragranular argon porosity for GA powders, which in some cases cannot be eliminated by subsequent cold or hot isostatic pressing methods and leads to weakening of mechanical properties of final parts.

Also, plasma rotating electrode process (PREP) is used for industrial production of spherical powders [14, 15]. In PREP process a plasma jet melts the surface layer of the rotating billet tip, and the melt is atomized by centrifugal forces [16, 17]. However, this method also has a number of significant limitations, because the operation of PREP equipment is associated with significant difficulties in obtaining a fraction of < 106 μm [18, 19]. To achieve a yield of this fraction of more than 40 wt.% there is a need to significantly increase the speed of billet rotation (more than 30.000 rpm), which complicates the already complex kinematic scheme of the PREP equipment (it is necessary to reduce the level of vibrations, design complex bearing systems, etc.) Also, this includes the difficulties associated with the

manufacture of a billet with precise dimensions, which must be polished with high accuracy [19].

In this aspect, there are prospects for obtaining spherical powders using technologies that use wires or rods as consumable materials, and the processes of heating, melting and dispersion of the melt are carried out by plasma jets without the use of centrifugal forces, high-speed equipment with a complex kinematic scheme [20–25]. Such technologies include the plasma arc atomization process, which is flexible and can be used to produce powders from a wide class of materials that are either produced by industry (wires, rods) or can be obtained in the form of ingots by foundry methods [26–30].

For the above-mentioned plasma-arc atomization technology, studying the mechanisms of melting, gas-dynamic and thermal interaction of the melt, forming at melting of the dispersed material, with the plasma jet, mechanisms of fragmentation of liquid metal drops, etc, is of considerable scientific and practical interest. These questions still remain practically unstudied, which is extremely necessary for further commercial application of the technology for manufacturing high-quality spherical powders from a wide range of materials [31–42]. It should be also noted that at present there are no approved mathematical models, which describe the processes of heating, melting and fragmentation of the melt, forming at the tips of flux-cored wires at plasma-arc atomization.

Therefore, the objective of the work is the theoretical and experimental study of the mechanisms and features of the processes of melting and fragmentation of the melt, forming at the tips of solid and flux-cored current-conducting wires, at the specified technological parameters of the process of plasma-arc atomization, where the following will be performed to achieve the posed objective:

1. Mathematical modeling of the process of melt formation and its fragmentation at plasma-arc atomization of solid and flux-cored wires, clarifying the regularities of fragmentation of the initial drops in the plasma jet, depending on atomization distance.

2. Experimental study of the mechanisms of fragmentation of the dispersed material of solid and flux-cored wires in the plasma jet, using high-speed filming and experimental procedure for determination of the powder particle size distribution (sieve analysis).

3. Comparison of the obtained theoretical and experimental data for assessment of the developed mathematical model.

4. Experimental study of the spheroidization process and peculiarities of microstructure formation of the powders, formed from solid and flux-cored wires during plasma-arc atomization.

MATERIALS AND METHODS

Procedure of atomization of solid and flux-cored wires and determination of the size of initial drops and fractional composition of atomization products

Technology of plasma-arc atomization of current-conducting solid and flux-cored wires (PTWA – plasma transferred wire arc) was used for experiment performance. It consists in melting the current-conducting wire-anode, introduced into the zone of high-speed plasma jet, and further refinement of the melt layer at the wire tip [43, 44]. This method envisages application of an accompanying gas flow directed coaxially to the plasma jet, which configures the latter, and promotes its compression, thus reducing the angle of opening of the atomized particle plume, increases the outflow velocity and the dynamic pressure of the plasma jet that in its turn creates the conditions for obtaining an optimal particle size distribution and chemical composition of the dispersed phase (Fig. 1). Plasma-arc atomization of solid and flux-cored wires was conducted in an argon atmosphere by the following procedure. Inert gas – argon was supplied for 20 min with the flow rate of 25 l/min from below the atomization chamber through the nozzle with a system of holes of 1.0 mm diameter (to ensure a laminar outflow of gas and to reduce the degree of air mixing with the supplied gas), in order to force air out of the chamber of volume V = 0.49 m^3, which was followed by atomization of wire materials in a controlled argon atmosphere.

Technological parameters of the process are as follows: current of 260 A, arc working voltage of 80–85 V, plasma-forming gas flow rate of 4.8 m^3/h, accompanying gas flow rate of 30 m^3/h, wire feed rate of 10–13.5 m/min. The distance from the tungsten electrode tip to the axis of the atomized wire is 14 mm. Plasma-forming and accompanying gas was argon of the higher grade I1 to ISO 14175-2008. Accepted atomization modes were determined by achievement of the minimal opening angle by the plasma jet and stability of the process at melting of the atomized wire in the plasma jet axial zone. Atomization distance was equal to 150 mm. Particle size distribution of the laboratory batches of powders was determined by the sieve analysis method in keeping with the procedure of ISO 2591-1:1988 [45–48] in impact sieve analyzer AS-200U (RO-TAP) (Ukraine) with a set of sieves with holes of sizes 25–500 μm, sample weight was not less than 200 g of powder.

Atomization material

Solid wire of 1.6 mm diameter from AISI 316L stainless steel and flux-cored wire of Fe-Al alloying system were used as atomization material (Table 1). Cored wire of Fe-Al system was
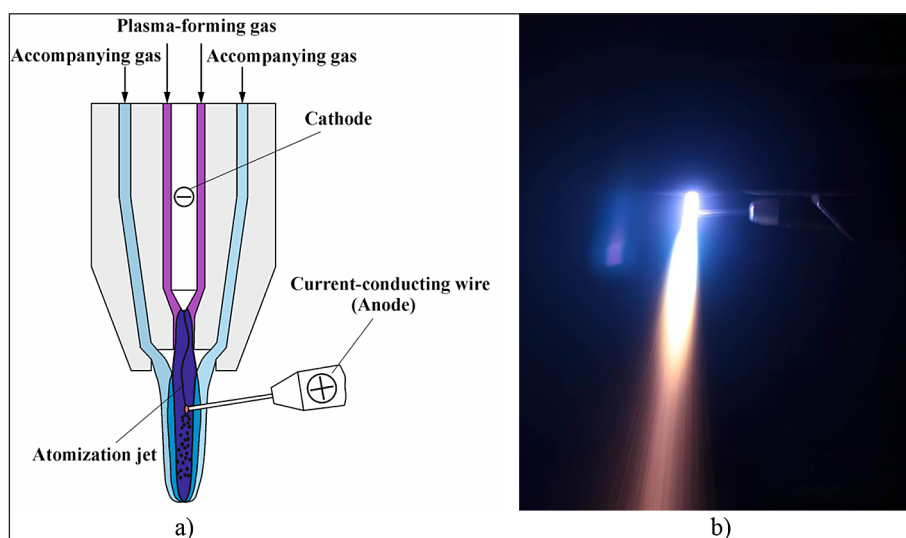
Figure 1. Schematic (a) and visualization (b) of PTWA atomization of 1.6 mm AISI 316L solid wire
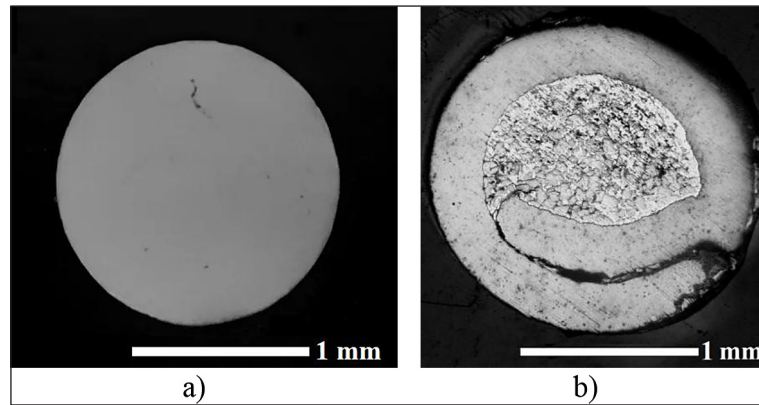
Figure 2. Cross-section of the solid AISI 316L (a) and flux-cored Fe-Al wires (b)

manufactured by the E.O. Paton Electric Welding Institute (Kyiv, Ukraine) and it consists of the sheath of AISI 1008 unalloyed steel with a thickness of 0.4 mm and aluminum (PA-4 grade) powder filler material with a filling ratio of 25–27 vol.%. It has a composition of 86 wt.% Fe + 14 wt.% Al, which corresponds to the formula of Fe_3Al intermetallic type.

Visualization of the atomization process

The photo was made with the camera PhotonFocus HD1-D1312-80-G2 (Switzerland) with 1312 × 1082 pixels CMOS detector and was provided with an optical bandpass filter (central wavelength 575 nm, FWHM 50 nm). The camera provided registration of monochromatic (brightness) images of a two-phase jet at 200-fps rate. Changeable lenses of the digital camera provided a spatial resolution of 22.4 and and 51.9 μm/pixel in the recorded frames.

Determination of the morphology and microstructure of powder particles

Morphology and microstructure of atomized powder particles was investigated with application of scanning electron microscope TESCAN MIRA3, VEGA3 LMU (Czech Republic) and further analysis of the obtained images in MIPAR program product, in order to study the morphology and microstructure of the atomized powder particles, using the procedure of [50–52].

Table 1. Chemical compositions of wires in wt.%

Wire	C	Si	Mn	Mo	P	S	Cr	Ni	N	Al	Fe
AISI 316L (solid)	0.03	1.0	2.0	2.0–2.5	0.045	0.015	16.5–18.5	10.0–13.0	0.1	-	base
Fe-Al (FCW)	-	-	-	-	-	-	-	-	-	14	base
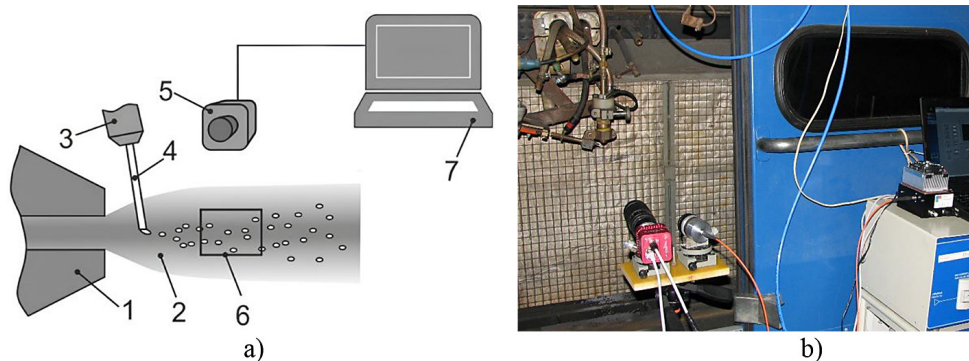
Figure 3. The spectral-brightness optical diagnostic system: (a) schematic diagram, (b) external appearance of the system during operation of the atomization facility: 1 – plasma torch nozzle; 2 - two-phase plasma jet; 3 – contact tip; 4 – atomized wire; 5 - camera, 6 – studied jet volume; 7 – computer [49]

Complex mathematical model of the process of plasma-arc atomization of current-conducting solid and flux-cored wires

Selection of the scheme of computational area of the process of plasma-arc atomization with current-conducting wire for mathematical modeling was performed using the approaches of [33, 40]. It was believed that the refractory cathode forms an annular electrode nozzle of radius R_c together with the channel wall (Fig. 4), through which the plasma-forming gas is supplied with flow rate G_1 and the total arc current I flows. Taken as the beginning of computational area was plane z = 0, located as a certain distance from the working end of the cathode. This allows considering the arc plasma flow in this plane axially symmetrical and one-dimensional in the direction of axis *OZ*. Shielding gas with flow rate G_2 is supplied through annular channel R_1… R_2 as an axially symmetric flow at angle α to the system axis of symmetry. Anode wire is located at distance Z_2 from the computational area beginning. It is assumed that arc current decreases smoothly in the region of anode attachment and a current-free inertial gas movement takes place further on (at z > Z_2). Under the impact of the anode spot of the
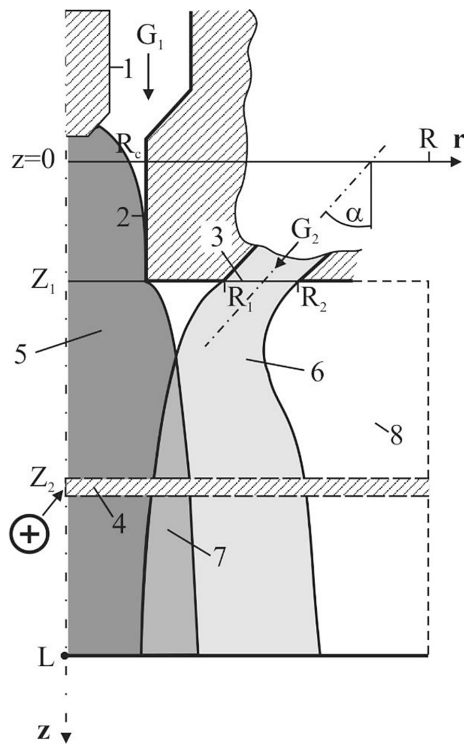
arc and the high-temperature plasma flow moving around the arc, the wire is heated and melted, and a layer of molten metal of characteristic thickness L_b forms at its tip. The molten wire material will be entrained by the plasma flow, forming a liquid metal jet. As it progresses further, this jet will break up into drops – dispersed particles of atomized material. Coming to the plasma flow, the molten particles are accelerated, heated and after reaching the critical conditions, they disintegrate with formation of finer fragments. Electric arc plasma flow and formation of a plasma jet under the conditions of plasma-arc atomization are described by a system of magnetohydrodynamic (MHD) equations in the approximation of a turbulent boundary layer for time average values of plasma temperature and velocity [30, 33]:

$$\frac{\partial}{\partial z}(\rho u) + \frac{1}{r}\frac{\partial}{\partial r}(r\rho\overline{v}) = 0 \tag{1}$$

$$\rho\left(u\frac{\partial u}{\partial z} + \overline{v}\frac{\partial u}{\partial r}\right) = \frac{1}{r}\frac{\partial}{\partial r}\left(r\overline{\eta}\frac{\partial u}{\partial r}\right) - \frac{\partial}{\partial z}\left(p + \mu_0\frac{H_\varphi^2}{2}\right) \tag{2}$$

$$\rho\,C_p\left(u\frac{\partial T}{\partial z} + v\frac{\partial T}{\partial r}\right) = \frac{1}{r}\frac{\partial}{\partial r}\left(r\overline{\chi}\frac{\partial T}{\partial r}\right) + \frac{\mathbf{j}^2}{\sigma} - \psi \tag{3}$$

where: T is the average plasma temperature; $\overline{v} = (\rho v + \rho' v')/\rho$, where v is the average radial velocity, ρ is the average plasma density, ρ' and v' are the pulsations of density and radial velocity of plasma; u is the average axial plasma velocity; p is the pressure; $C_p(T,p)$ is the specific heat at constant pressure; σ is the specific electric conductivity of plasma; $\psi(T,p)$ is the volume power density of intrinsic radiation power; j is the vector of electric current density; $\overline{\eta}$ and $\overline{\chi}$ are the full coefficients of dynamic viscosity and heat conductivity of plasma, which are sums of the molecular and turbulent viscosities and heat conductivity, respectively; μ_0 is the universal magnetic constant; H_φ is the azimuthal component of the arc current magnetic field, which is related to the component of electric field density by the following relationships:

$$j_z = \frac{1}{r}\frac{\partial}{\partial r}(rH_\varphi); \; j_r = -\frac{\partial H_\varphi}{\partial z} \tag{4}$$

The electromagnetic characteristics of the arc are described using the equation of magnetic field intensity of the arc current:

Figure 4. Scheme of computational area: 1 – cathode; 2 – plasmatron nozzle, 3 – channel of accompanying gas flow blowing the plasma jet; 4 – wire-anode; 5 – arc plasma; 6 – accompanying gas; 7 – mixing zone; 8 – external gas medium

$$\frac{\partial}{\partial r}\left[\frac{1}{r\sigma}\frac{\partial(rH_\varphi)}{\partial r}\right]+\frac{\partial}{\partial z}\left[\frac{1}{\sigma}\frac{\partial H_\varphi}{\partial z}\right]=0 \qquad .$$

The equation of convective diffusion of plasma-forming gas in the external gas atmosphere is used to allow for the convective diffusion processes occurring at mixing of plasma-forming gas with the external gas atmosphere, and respective change of the composition, thermophysical properties and plasma transfer coefficients:

$$\rho\left(u\frac{\partial m_1}{\partial z}+\overline{v}\frac{\partial m_1}{\partial r}\right)=\frac{1}{r}\frac{\partial}{\partial r}\left(r\rho\overline{D}_{12}\frac{\partial m_1}{\partial r}\right)$$

$$m_1+m_2=1. \qquad (5)$$

where: $m_1(r,z)$ and $m_2(r,z)$ are the relative weight concentrations of plasma-forming and external gas in the plasma mixture, $\overline{D}_{12}$ is the coefficient of binary diffusion.

The system of MHD equations together with accompanying relationships, k-ε turbulence model and boundary and initial conditions completely defines the thermal and gas-dynamic characteristics of the turbulent plasma flow, both in the arc and inertial sections of the flow. These equations form the basis of a unified mathematical model suitable for calculation of spatial distributions of temperature and velocity of subsonic turbulent plasma flows, which are generated in our case by the plasmatron with a partially open arc in the presence of an accompanying gas flow, moving around the plasma arc.

The thermal state of the current-conducting solid and flux-cored wires at plasma-arc atomization was determined using models [40, 53–57], based on a quasi-stationary equation of heat conductivity presented in the cylindrical system of coordinates:

$$\gamma_w C_w v_w \frac{\partial T_w}{\partial z_w}=\frac{1}{r}\frac{\partial}{\partial r}\left(\chi_w r\frac{\partial T_w}{\partial r}\right)+\frac{\partial}{\partial z_w}\left(\chi_w\frac{\partial T_w}{\partial z_w}\right)+j^2\rho_w \quad (6)$$

where: T_w (r,z_w) is the spatial distribution of temperature in the wire; ρ_w (T) γ_w (T), C_w (T), χ_w (T) are the density, specific heat, coefficient of heat conductivity and specific electric resistance of wire material, respectively; j is the electric current density.

Boundary conditions for Equation 6 are set, allowing for the convective-conductive heat exchange of the plasma flow and ambient gas with the wire side surface Q_c; heat exchange of thermal radiation energy between the plasma and wire surface

Q_r; action of the electric arc contributing the heat though the anode spot at the wire tip Q_a; volume Joule heating of the wire by flowing electric current; heat losses with the molten metal carried away by the plasma flow Q_t, as well as cooling of the wire surface due to the vapour flow removing the energy of wire material atom evaporation energy Q_v. Equation 6 is closed by relationships, allowing determination of the spatial position of the wire tip relative to the plasma jet axis $L_p = z^*$, at which the volume of liquid layer held at the wire tip V_b will correspond to the wire molten metal volume $V_{liq}=\pi R_w^2 L_{liq}$, i.e. condition $V_b = V_{liq}$ will be satisfied. For the case of heating and melting of flux-cored wire (Fig. 5), at contact of two media - the steel sheath with the powder core, the molten part of the wire with the unmolten part, boundary conditions of the IVth of the following form were used:

$$T_1(R_c-\varepsilon,z,t)=T_2(R_c+\varepsilon,z,t) \qquad (7)$$

$$\lambda_1\frac{\partial T_1}{\partial r}\bigg|_{r=R_c}=\lambda_2\frac{\partial T_2}{\partial r}\bigg|_{r=R_c}, \text{ where } \varepsilon\to 0.$$

To describe the thermophysical parameters and transfer coefficients of the wire powder core we will use approaches applied at modeling the heat transfer processes in porous media, in particular, application of effective heat capacity, heat conductivity, etc. which are determined by ratios of the following kind:

$$\lambda=\phi\cdot\lambda_s+(1-\phi)\cdot\lambda_p \qquad (8)$$

All the other boundary conditions correspond to the earlier proposed model of wire heating and melting at plasma-arc atomization [53]. In order to determine the spatial position of the wire, as well as the parameters of the melt held at the wire tip, approaches were used, which were described in works [33, 53–63]. Here, the scope of the wire molten part will be determined by the volumes of molten particles of the wire sheath and the powder core. Flowing of the melt trickle from the tip of the current-conducting wire and formation of dispersed particles during atomization is described with sufficient accuracy by a quasi-unidimensional system of Navier-Stoke's equations, written allowing for the force of viscous impact on the melt from the plasma flow side:

$$\frac{\partial v}{\partial t}+v\frac{\partial v}{\partial z}=-\frac{1}{\rho_w}\frac{\partial p}{\partial z}+3\upsilon_w\frac{1}{h^2}\frac{\partial}{\partial z}\left(h^2\frac{\partial v}{\partial z}\right)-\frac{2\tau_p}{h\gamma_w}, \quad (9)$$

$$-L_d<z<0;$$
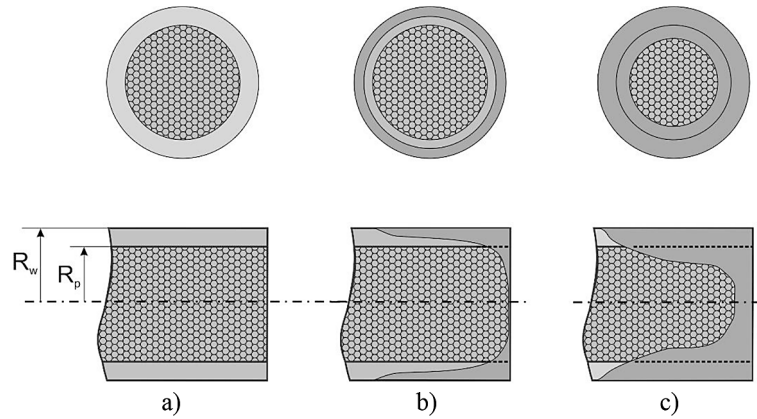
Figure 5. Stages of melting of flux-cored wire with a steel sheath: a – initial state; b – partially melted sheath; c – molten sheath with partially melted core

$$\frac{\partial F}{\partial t} + \frac{\partial (vF)}{\partial z} = 0, \qquad (10)$$

where: $v=v(z,t)$ is the axial component of the melt flow velocity; $p = 2\sigma K + p_{ext}$ is the capillary pressure, σ is the surface tension coefficient; K is the average curvature of the jet surface, p_{ext} is the pressure in the external medium; $h=h(z,t)$ is the radius of the jet cross-section; $F(z,t)=\pi h^2(z,t)$ is the cross-sectional area of the jet; $\tau_p = \tau_p(z)$ is the stress of friction in the plasma on the flown-around surface; γ_w, ν_w are the density and kinematic viscosity of the wire material at the melting temperature; L_d is the jet length.

After the drop separation, its movement in the plasma jet is described by the following equations [30, 40, 51, 53–66]:

$$\frac{d(m\mathbf{w})}{dt} = \mathbf{F}; \qquad \frac{d\mathbf{r}}{dt} = \mathbf{w}. \qquad (11)$$

where: $m(t)$, $w(t) = (w_x, w_y, w_z)$ and r $(t) = (x, y, z)$ are the current values of mass, velocity vector and radius-vector of the particle position in the selected Cartesian system of coordinates; F(t) is the resultant force acting on the liquid particle from the plasma side. Equation 11 is complemented by the relationships allowing for deformation of the molten particles during their movement in the plasma flow, as well as expressions allowing for appearance of the critical conditions of breaking up and formation of fragments resulting from particle fragmentation that is well

described in works [33, 53]. In its turn, the thermal state of particles in the plasma flow was determined using a non-stationary equation of heat conductivity, taking into account the assumption of the spherical shape of the particle:

$$\rho_m \overline{C}_m \frac{\partial T_m}{\partial t} = \frac{1}{r^2} \frac{\partial}{\partial r}\left(r^2 \chi_m \frac{\partial T_m}{\partial r} \right). \qquad (12)$$

where: $T_m(r, t)$ is the space-time distribution of temperature in the particle; χ_m (T) and $\overline{C}_m(T)$ are the coefficient of heat conductivity and effective heat capacity of its material. Boundary conditions for Equation 12 are written allowing for the convective-conductive and radiation heat flows, as well as specific heat losses associated with surface evaporation of the particle material [33].

RESULTS AND DISCUSSION

Modeling

The developed physico-mathematical model and software for its computer realization was used to conduct the numerical analysis of the characteristics of the flow of turbulent argon plasma generated by the plasmatron with a consumable current-conducting anode [33, 51, 53–66]. It was found that blowing of turbulent plasma jet by a flow of cold gas with flow rate $G_2 = 30$ m^3/h prevents jet expansion and significantly increases its length, compared to the submerged jet (Fig. 6, 7). Submerged jet of argon arc plasma outflowing
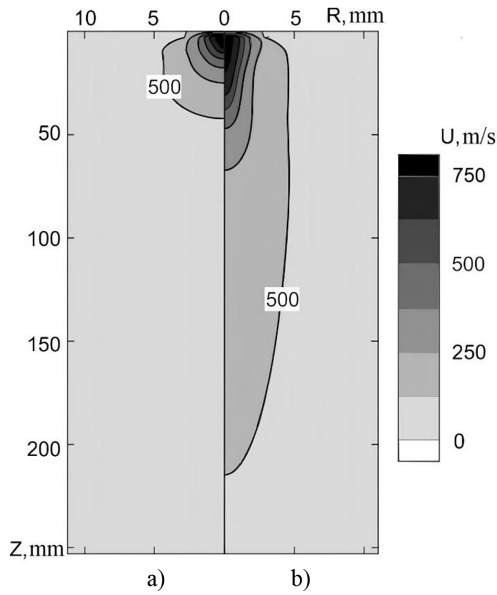
Figure 6. Distribution of axial velocity of the plasma jet outflowing into the ambient atmosphere: a) without blowing; б) with blowing; $I = 260$ A, $G_1 = 4.8$ m³/h, $G_2 = 30$ m³/h

Figure 7. Temperature distribution of the plasma jet outflowing into the ambient atmosphere: (a) without blowing; (b) with blowing; $I = 260$ A, $G_1 = 4.8$ m³/h, $G_2 = 30$ m³/h

into the ambient atmosphere, rather quickly mixes with it, cooling much more intensively than the flown-around jet.

Here, the extent of the high-temperature high-velocity zone ($Z < 60$ mm) is greatly increased. According to the conditions of plasma-arc atomization technology, it is rational to introduce the atomized wires into this zone, as here the jet velocity and temperature reach the highest values of 750–600 m/s and 20 000–15 000 °K, respectively. It leads to the fact that the melt forming at melting of the atomized wire tip will be exposed to significant gas-dynamic impact of the plasma jet in this zone, and this will cause its fragmentation with formation of a large number of finer particles (secondary fragmentation).

The developed physical-mathematical model of the thermal state of current-conducting wire [48] was used to determine the parameters of the liquid layer held at the wire tip (Fig. 8). It was found that at atomization of the solid wire in the specified atomization mode the wire will take up a position with 0.4–1.0 mm shifting from the plasma jet axis, and at atomization of the flux-cored wire - with 0.5–1.3 mm shifting, but the thickness of the liquid layer is equal to 0.1–0.16 mm for both the cases. Numerical studies using approaches of [33, 53, 58, 64] were conducted on the base of the model of molten particle behaviour in the plasma flow, and distribution of particles formed as a result of

fragmentation by velocities, temperatures and sizes at the distance $z = 140$ mm from the plasmatron nozzle edge was obtained (Fig. 9).

As one can see from calculation data shown in Fig. 9, at plasma-arc atomization of 1.6 mm solid wire from AISI 316L stainless steel and 1.8 mm flux-cored wire of Fe-Al system multiple disintegration of the particles and their fragments, moving in the plasma jet, takes place. Initial drops of average diameter of 670 µm form at the tip of atomized solid AISI 316L wire, and at 150 mm distance fragments (particles) of average diameter of 105 µm form as a result of multiple disintegration, while for flux-cored wire of Fe-Al system the initial diameter of the drops is equal to 780 µm at average diameter of fragments of 125 µm. Analysis of calculation results showed that the
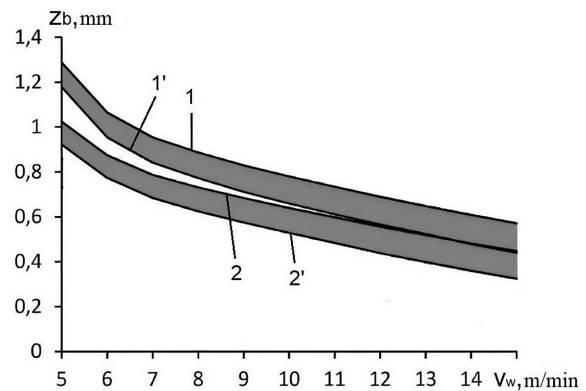
Figure 8. Influence of the wire feed rate on its position relative to the plasma jet axis (1–2) and thickness of the liquid layer (1'–2') held at the tip at atomization of flux-cored 1, 1' and solid 2, 2' wires
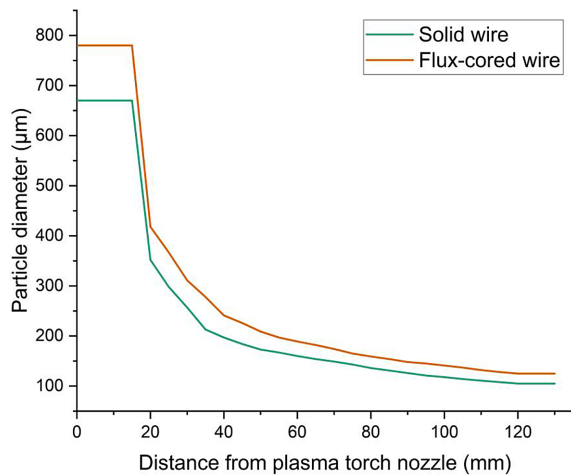
Figure 9. Change of average diameter (d) of the particles forming at the tip of atomized solid AISI 316L wire and flux-cored wire of Fe-Al system during plasma-arc atomization, depending on the distance from plasmatron edge (z)

most characteristic two areas of disintegration of the liquid particles and their fragments exist at the above-mentioned atomization distance. The most intensive particle disintegration takes place in the first area (near the plasmatron nozzle edge) of the length of the order of 60 mm, characterized by high values of plasma velocity and temperature in the considered modes of plasma-arc atomization. In this area We number for the particles is significantly higher than the critical value of Weber number, leading to their intensive disintegration. In the second area the conditions of the particle

flowing around change due to reduction of particle sizes (as a result of disintegration), as well as lowering of the relative velocity of plasma and particles when moving away from the plasmatron nozzle edge. Here, the molten particles feel the smooth increase of the force of aerodynamic resistance, due to a change in their shape that leads to their breaking up after a certain time. Particle disintegration practically stops at the distance of approximately 120 mm from the plasmatron nozzle edge, as a result of a significant reduction of the force of aerodynamic impact of the plasma flow on the molten particles and increase of the surface tension force at their partial solidification at the mentioned distance that, in its turn no longer leads to their deformation and breaking up.

Experimental data

One of the important objectives of this study is visualization of the process of melt formation and drop separation from the tip of atomized wire, as well as its movement and disintegration with formation of dispersed fragments, as a result of the action of the aerodynamic force of the plasma jet that allows determination of the initial dimensions of the drops, nature of disintegration, comparing the obtained experimental data with the calculated data and assessing the adequacy of the developed model. Earlier the means of mathematical modeling and experimental studies [17, 49–52, 58, 67] revealed that at high-velocity
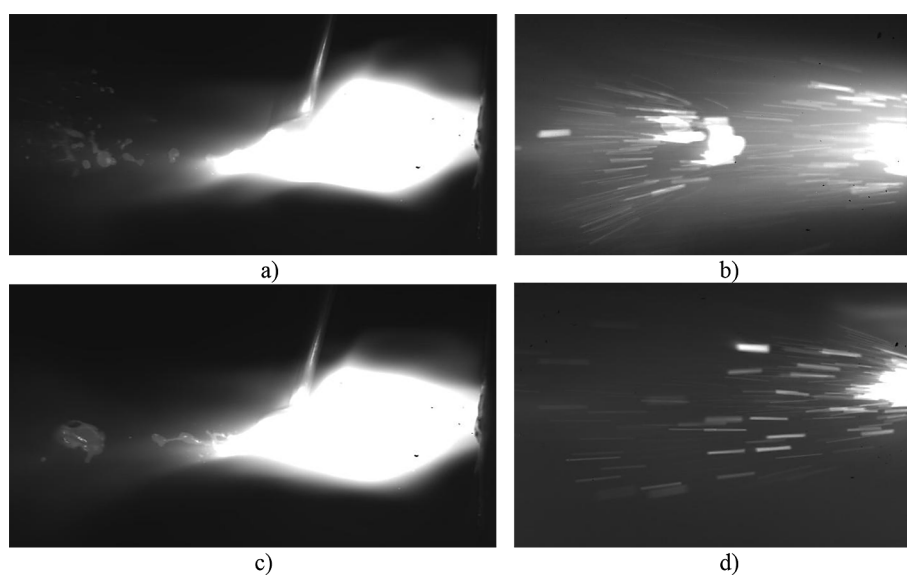
Figure 10. Visualization of the processes of fragmentation of the initial (a, b) and secondary (c, d) drops, forming during plasma-arc atomization of solid AISI 316L wire (a, c) and flux-cored wire of Fe-Al system (b, d) at the current of 260 A

plasma-arc atomization the jet metal transfer is the main type of breaking up of the jet of molten metal separating from the wire tip (Weber number of 12 < We < 40–100), at which the initial drops disintegrate into a large number of fine fragments of practically the same size (secondary drops). Fig. 10 gives the photos obtained at high-speed filming of the process of plasma-arc atomization of both the solid and flux-cored wires, which fully coincide with mathematical modeling results. Thus, analysis of the photos showed (Fig. 4 a), that in both the cases in the specified atomization modes (at high plasma-forming gas flow rates) the melt forming at the atomized wire tip is elongated in a jet of 2–5 mm length, and then disintegrates into drops of practically the same size. However, for the case of atomization of solid wire of AISI 316L grade, the initial drop diameter is equal to 720 µm, and for atomization of flux-cored Fe-Al wire it is 815 µm. Analysis of the obtained images showed that secondary fragmentation of the melt is performed by the mechanism of disintegration of «bag breakup» or «bag/streamer breakup» type with Weber numbers in

the range of 12 < We < 40–100, in keeping with the published data [33, 49].

Determination of the dimensions of secondary fragments (powder) by the methods of sieve analysis showed that at the same modes of plasma-arc atomization of the studied current-conducting solid and flux-cored wires the particle size distribution is in the range from 1 to 400 µm in the general case. For both the cases the main fraction is 1-300 µm, which is equal up to 98 wt.% for atomization of solid stainless wire of AISI 316L grade, and in the case of atomization of flux-cored wire of Fe-Al system it is up to 96 wt.%, and the average particle diameter is 119 and 142 µm, respectively. Fig. 11 (a, b) shows a SEM image and microstructure of powder produced at plasma-arc atomization of solid wire of AISI 316L grade and flux-cored wire of Fe-Al system. Analysis of the powder morphology in MIPAR showed that in both the cases of atomization of solid AISI 316L wire the powder has a spherical shape with average sphericity factor S = 0.87, and in the case of atomization of flux-cored Fe-Al wire – S = 0.78. At the same time, the amount of external defects
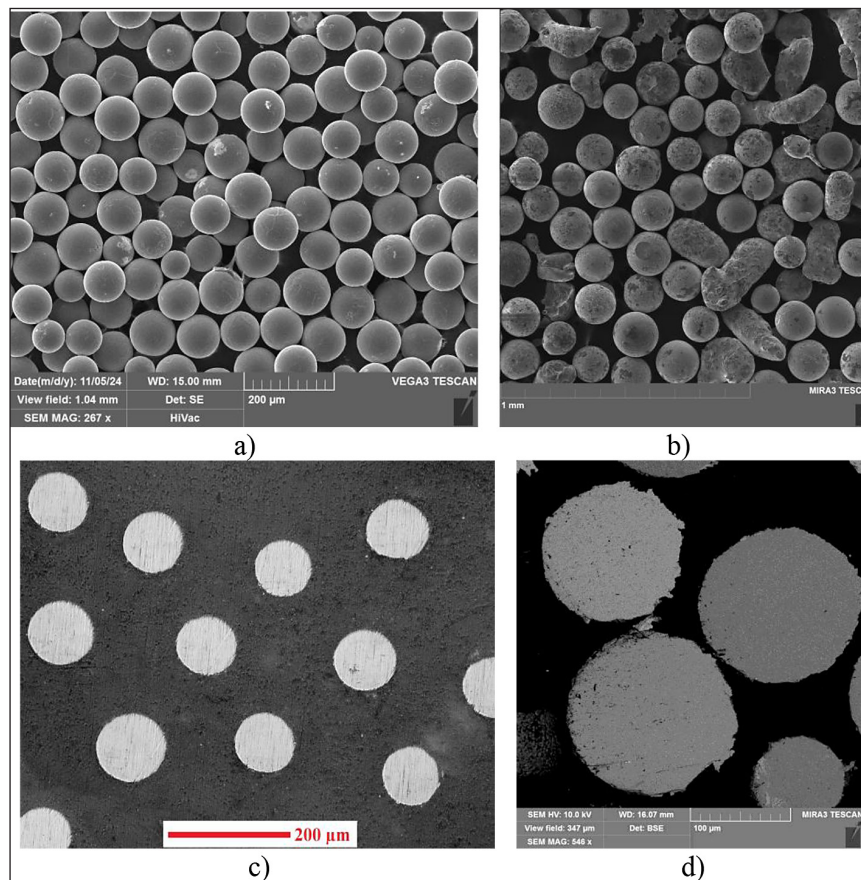
Figure 11. Morphology (a, b) and microstructure (c, d) of powder produced at plasma-arc atomization of solid AISI 316L wire (a, c) and flux-cored wire of Fe-Al system (b, d) at 260 A current

in the form of satellites is not observed on both powders, and the amount of irregularly shaped particles for AISI 316L powder is no more than 1 wt.% and for Fe-Al powder no more than 7 wt.%. Analysis of cross-sectional images Fig. 11 (c, d) of powders obtained in the plasma-arc atomization process showed that their microstructure is characterized by the absence of pores and voids.

Comparison of the results

Calculation of the dimensions of initial drops separating from the atomized wire tips showed that the error between the theoretical and experimental data for solid sire of AISI 316L grade is not higher than 3 %, where the average diameter is equal to 650 and 670 µm, respectively, and for flux-cored wire of Fe-Al system it is not higher than 7 % at average diameter of 730 and 780 µm, respectively. Analyzing the calculated and experimental data on particle size distribution of powder produced at powder-arc atomization of the studied solid and flux-cored wires (Fig. 12), one can see that in both the cases the main fraction is that of 5–300 µm, which makes up to 97% of the total powder weight, the amount of particles of 300-400 µm fraction is at a rather low level, being not higher than 3 wt.%. At more detailed consideration of fractional composition of atomized particles, it should be noted that the error between the theoretical and experimental data for 1–100 µm fraction is equal to not more than 16%, and for 100–200 µm fractions it is not more than 7%, respectively. For 200–300 µm fraction the error of the results becomes much greater and is equal to 32% and for 300–400 µm fraction it is equal to 62%, respectively. The above-given

data show that for calculation of the main fraction the error between the theoretical and experimental results is not higher than 32% that allows prediction of fractional composition with pretty good accuracy. It should be also noted that the share of the coarse fraction of 300–400 µm in the total volume is small, so that it does not have any essential influence on the general change of the particle size distribution.

The high sphericity coefficient of 0.78–0.87 for both powders indicates that the powders undergo a sufficient degree of spheroidization. Complete spheroidization is achieved when the spheroidization time exceeds the solidification time of the droplet, during which time the high surface energy of the molten droplets promotes the formation of spherical particles before they solidify. However, it should be noted that the lower sphericity coefficient for Fe-Al powder may be due to the melting peculiarities of flux-cored wires, which are different from solid wires. Thus, at plasma-arc atomization of Fe-Al powder the process of spheroidization may not occur completely due to the rapidity of the process, high cooling rates of the formed fragments, which have large sizes in comparison with solid wires. Also, in this case, a significant role is played by the surface state of the powder filler material - aluminum, on which an oxide film is formed, which also contributes to the decreasing of sphericity and increase in the number of irregularly shaped particles.

The absence of pores and voids in the powder suggests that the solidification rate for both powders is moderate, as the gas either does not enter the powder or escapes in time. This is in contrast to the gas atomization process, where the gas is forced into the powder as it solidifies [68].
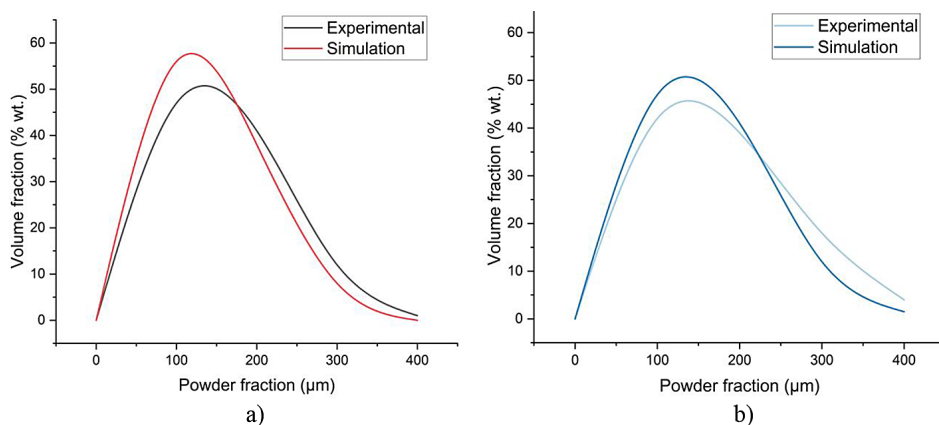
Figure 12. Histograms of particle size distribution in the powder produced at plasma-arc atomization of solid AISI 316L wire (a) and flux-cored wire of Fe-Al system at 260 A current

Because the solidification rate is too high, the gas output rate is too low to get out, thus it gets wrapped up inside the powder, forming internal pores and voids [69].

CONCLUSIONS

Mathematical modeling of the processes of thermal and dynamic interaction of the plasma jet with the melt, forming at the tips of solid and flux-cored wires at plasma-arc atomization was performed. Size distribution was determined of particles forming as a result of melt fragmentation at the tips of solid and flux-cored wires under the aerodynamic influence of the plasma jet for different parameters of the plasma-arc atomization process. Modeling results showed that at the tip of atomized solid AISI 316L wire initial drops with average diameter close to 670 µm are formed, and at 150 mm distance fragments (particles) of average diameter of 105 µm form as result of multiple disintegration, whereas for flux-cored wire of Fe-Al system the initial drop diameter is equal to 780 µm at average fragment diameter of 125 µm. Theoretical calculations of the process of flux-cored wire melting at the specified mode showed that in this case the dimensions of the initial drops greater by 16 % are associated with the wire shifting by 0.4 mm from the plasma jet axis, that promotes formation of initial drops of larger dimensions, as melt fragmentation occurs in the zone of lower gas-dynamic pressure.

Dimensions of the initial drops, forming at the tips of atomized wires were determined experimentally using high-speed filming. It was established that for the case of atomization of the solid stainless wire of AISI 316L grade, the average dimensions of the initial drops are equal to 720 µm, and for atomization of flux-cored Fe-Al wire they are 815 µm. Determination of fragment dimensions at atomization distance of 150 mm by sieve analysis procedure showed that in the same modes of plasma-arc atomization of the studied current-conducting solid and flux-cored wires the particle size distribution range is from 1 to 400 µm. For both the cases, the main fraction is 1–300 µm, which is up to 98 wt. % for atomization of solid stainless wire of AISI 316L grade, and in the case of atomization of flux-cored wire of Fe-Al system it is up to 96 wt.%, and the average particle diameter being 119 and 142 µm, respectively.

Comparison of the obtained experimental and calculation data showed that the 1–300 µm fraction, equal to 96–99 wt.% is the main fraction for atomization of both the solid stainless wire of AISI 316L grade, and flux-cored wire of Fe-Al system. Here, the error between the theoretical and experimental data for calculation of the main fraction is not higher than 16–32% that is indicative of their quite satisfactory correspondence, and enables prediction of the powder fractional composition in order to determine the optimal modes of the process of plasma-arc atomization of a wide range of wire materials. Experimental study of the spheroidization process and the features of the microstructure formation of plasma-arc atomized powders from different types of wires showed that generally high-quality spherical powders with a sphericity coefficient close to 0.8–0.9 and the absence of internal defects in the form of pores and voids are formed. At the same time, the lower sphericity coefficient and the higher number of irregularly shaped particles is due to high cooling rates of the formed fragments, which have large sizes in comparison with solid wires and surface state of powder filler material.

REFERENCES

1. Nguyen H., Pramanik A., Basak A. et al. A critical review on additive manufacturing of Ti-6Al-4V alloy: microstructure and mechanical properties. Journal of Materials Research and Technology. 2022. (18), 4641–4661. https://doi.org/10.1016/j.jmrt.2022.04.055

2. Ahn D. Directed energy deposition (DED) process: State of the art. Int. J. of Precis. Eng. and Manuf.-Green Tech. 2021. (8), 703-742. https://doi.org/10.1007/s40684-020-00302-7

3. Svetlizky D., Das M., Zheng B. et al. Directed energy deposition (DED) additive manufacturing: Physical characteristics, defects, challenges and applications. Materials Today. 2021. (49), 271–295. https://doi.org/10.1016/j.mattod.2021.03.020

4. King W., Anderson A., Ferencz R. et al. Laser powder bed fusion additive manufacturing of metals; physics, computational, and materials challenges.

Applied Physics Reviews. 2015. (2), 041304. https://doi.org/10.1063/1.4937809

5. Fatemeh A, Haydari Z., Salehi H. et al. Spreadability of powders for additive manufacturing: A critical review of metrics and characterization methods. 2024. Particuology. (93), 211–234. https://doi.org/10.1016/j.partic.2024.06.013

6. Olakanmi E. Selective laser sintering/melting (SLS/SLM) of pure Al, Al–Mg, and Al–Si powders: Effect of processing conditions and powder properties. Journal of Materials Processing Technology. 2013. (213), 1387–1405. https://doi.org/10.1016/j.jmatprotec.2013.03.009

7. Attar H., Prashanth K., Zhang L. et al. Effect of powder particle shape on the properties of in situ Ti–TiB composite materials produced by selective laser melting. Journal of Materials Science & Technology. 2015. (31), 1001–1005. https://doi.org/10.1016/j.jmst.2015.08.007

8. Drawin S., Deborde A., Thomas M. et al. Atomization of Ti-64 alloy using the EIGA process: comparison of the characteristics of powders produced in labscale and industrial-scale facilities. MATEC Web of Conferences 2020. (321), 07013. https://doi.org/10.1051/matecconf/202032107013

9. Xiao H., Gao B., Yu S. et al. Life cycle assessment of metal powder production: a Bayesian stochastic Kriging model-based autonomous estimation. Auton. Intell. Syst. 2024. (4), 20. https://doi.org/10.1007/s43684-024-00079-5

10. Chen G., Zhao S., Tan P. et al. A comparative study of Ti-6Al-4V powders for additive manufacturing by gas atomization, plasma rotating electrode process and plasma atomization. Powder Technology. 2018. (333), 38–46. https://doi.org/10.1016/j.powtec.2018.04.013

11. Sun P., Fang Z., Zhang Y. et al. Review of the methods for the production of spherical Ti and Ti alloy powder. JOM. 2017. (69), 1853–1860. https://doi.org/10.1007/s11837-017-2513-5

12. Korzhyk V., Strohonov D., Burlachenko O. et al. Development of plasma-arc technologies of spherical granule production for additive manufacturing and granule metallurgy. The Paton Welding J. 2023. (12), 3–18. https://doi.org/10.37434/tpwj2023.12.01

13. Yurtukan E., Unal R. Theoretical and experimental investigation of Ti alloy powder production using low-power plasma torches. Transactions of Nonferrous Metals Society of China. 2022. (32), 175-191. https://doi.org/10.1016/S1003-6326(21)65786-2

14. Zhao Y., Cui Y., Numata H. et al. Centrifugal granulation behavior in metallic powder fabrication by plasma rotating electrode process. Sci Rep. 2020. (10), 18446. https://doi.org/10.1038/s41598-020-75503-w

15. Cui Y., Zhao Y., Numata H. et al. Effects of plasma rotating electrode process parameters on the particle size distribution and microstructure of Ti-6Al-4 V alloy powder. Powder Technology. 2020. (376), 363–372. https://doi.org/10.1016/j.powtec.2020.08.027

16. Cui Y., Zhao Y., Numata H. et al. Effects of process parameters and cooling gas on powder formation during the plasma rotating electrode process. Powder Technology. 2021. (393), 301–311. https://doi.org/10.1016/j.powtec.2021.07.0624

17. Han Z., Zhang P., Lei L. et al. Morphology and particle analysis of the Ni$_3$Al-based spherical powders manufactured by supreme-speed plasma rotating electrode process. Journal of Materials Research and Technology. 2020. 6(9), 13937–13944. https://doi.org/10.1016/j.jmrt.2020.09.102

18. Zhang Y., Song M., Li Y. et al. Effect of preparation process on the microstructure and characteristics of TiAl pre-alloyed powder fabricated by plasma rotating electrode process. Crystals. 2024. (14), 562. https://doi.org/10.3390/cryst14060562

19. Korzhyk V., Kulak L., Shevchenko V. et al. New equipment for production of super hard spherical tungsten carbide and other high-melting compounds using the method of plasma atomization of rotating billet. Materials Science Forum. 2017. (898), 1485–1497. https://doi.org/10.4028/www.scientific.net/msf.898.1485

20. Qiu J., Yu D., Qu Y. et al. In-flight droplet plasma atomization: A novel method for preparing ultrafine spherical powders. Advanced Powder Technology. 2025. 1(36), 104757. https://doi.org/10.1016/j.apt.2024.104757

21. Zhang Q., Yu D., Liu F. et al. Modeling on the size of the pre-breaking molten droplet in plasma atomization for controlling the size of the produced powders. Applied Thermal Engineering. 2023. (232), 121031. https://doi.org/10.1016/j.applthermaleng.2023.121031

22. Bobzin K., Wietheger W., Burbaum E. et al. High-velocity arc spraying of fe-based metallic glasses with high si content. J Therm Spray Tech. 2022. (31), 2219–2228. https://doi.org/10.1007/s11666-022-01433-w

23. Yin Z., Yu D., Zhang Q. et al. Experimental and numerical analysis of a reverse-polarity plasma torch for plasma atomization. Plasma Chem Plasma Process. 2021. (41), 1471–1495 https://doi.org/10.1007/s11090-021-10181-8

24. Ozerskoi N., Silin A., Razumov N. et al. Optimization of EI961 steel spheroidization process for subsequent use in additive manufacturing: Effect of plasma treatment on the properties of EI961 powder. Reviews Adv. Mater. Sci. 2021. 60(1), 936–945. https://doi.org/10.1515/rams-2021-0078

25. Lagutkin S., Achelis L., Sheikhaliev S., Uhlenwinkel V., Srivastava V. Atomization process for metal powder. Mater. Sci. Eng.: A. 2004. 383(1), 1–6. https://doi.org/10.1016/j.msea.2004.02.059

26. Gu Y., Xu Y., Shi Y., Feng C., Volodymyr K. Corrosion resistance of 316 stainless steel in a simulated pressurized water reactor improved by laser cladding with chromium. Surface and Coatings Technology. 2022. (441), 128534. https://doi.org/10.1016/j.surfcoat.2022.128534

27. Korzhyk V., Khaskin V., Grynyuk A. et al. Comparing features in metallurgical interaction when applying different techniques of arc and plasma surfacing of steel wire on titanium. Eastern-European Journal of Enterprise Technologies. 2021. 12(112), 6–17. https://doi.org/10.15587/1729-4061.2021.238634

28. Chen G., Zhao S., Tan P. et al. A comparative study of Ti–6Al–4V powders for additive manufacturing by gas atomization, plasma rotating electrode process and plasma atomization. Powder Technol. 2018. (333), 38–46. https://doi.org/10.1016/j.powtec.2018.04.013

29. Dharmanto A., Sugeng S., Supriadi B. New design of conduit plasma atomization for fabricating spherical metal powder and its optimization using design of experiments method. Powder Metall. Met. Ceram. 2022. (60), 531–545. https://doi.org/s11106-022-00266-0

30. Fialko N., Prokopov V., Meranova, N. et al. Temperature conditions of particle-substrate systems in a gas-thermal deposition process. Fizika i Khimiya Obrabotki Materialov. 1994. (2), 59–67.

31. Korzhik V. Theoretical analysis of the conditions required for rendering metallic alloys amorphous during gas-thermal spraying. III. Transformations in the amorphous layer during the growth process of the coating. Powder Metall. Met. Ceram. 1992. 31(11), 943–948. https://doi.org/10.1007/BF00797621

32. Kharlamov M., Krivtsun I., Korzhyk V. Dynamic Model of the Wire Dispersion Process in Plasma-Arc Spraying. Journal of Thermal Spray Technology. 2014. (23), 420–430. https://doi.org/10.1007/s11666-013-0027-4

33. Li H., Chen X. Three-dimensional simulation of a plasma jet with transverse particle and carrier gas injection. Thin Solid Films. 2001. (390), 175–180. https://doi.org/10.1016/S0040-6090(01)00915-4

34. Remesh K., Yu S., Ng H. et al. Computational study and experimental comparison of the in-flight particle behavior for an external injection plasma spray process. Journal of Thermal Spray Technology. 2003. 12(4), 508–522. https://doi.org/10.1361/105996303772082251

35. Michaelides E. Particles, bubbles and drops: Their motion, heat and mass transfer. World Scientific Publ. 2006. 424. https://doi.org/10.1142/6018

36. Guildenbecher D., Lopez-Rivera C., Sojka P. Secondary atomization. Exp. Fluids. 2009. 46(3), 371–402. https://doi.org/10.1007/s00348-008-0593-2

37. Mariaux G., Vardelle A. 3-D time-dependent modeling of the plasma spray process. Part 1: flow modeling. International Journal of Thermal Sciences. 2005. (44), 357–366. https://doi.org/10.1016/j.ijthermalsci.2004.07.006

38. Voitcu G., Echim M. Transport and entry of plasma clouds/jets across transverse magnetic discontinuities: Three-dimensional electromagnetic particle-in-cell simulations. Journal of Geophysical Research: Space Physics. 2016. (121), 4343–4361 https://doi.org/10.1002/2015JA021973

39. Marchetti J., Patruno L., Jakobsen H. Mathematical framework for higher-order breakage scenarios. Chemical Engineering Science. 2010. (65), 5881–5886. https://doi.org/10.1016/j.ces.2010.08.008

40. Hu J., Tsai H. Heat and mass transfer in gas metal arc welding. Part I: The Arc. Int. J. Heat and mass transfer. 2007. 50(5–6), 833–846. https://doi.org/10.1016/j.ijheatmasstransfer.2006.08.025

41. Hill P., Ng K. Statistics of multiple particle breakage. AIChE. 1996. (42), 1600–1611. https://doi.org/10.1002/aic.10091

42. Hryhorenko G., Adeeva L., Tunik A. et al. Formation of microstructure of plasma-arc coatings obtained using powder wires with steel skin and B_4C + $(Cr, Fe)_7C_3$ + Al filler. Metallofizika i Noveishie Tekhnologii. 2020. 42(9), 1265–1282. https://doi.org/10.15407/mfint.42.09.1265

43. Hryhorenko G., Adeeva L., Tunik A. et al. Structurization of coatings in the plasma arc spraying process using B4C + (Cr, Fe)7C3-cored wires. Powder Metall. Met. Ceram. 2019. 58(5–6), 312–322. https://doi.org/10.1007/s11106-019-00080-1

44. ISO 2591-1:1988 «Test sieving — Part 1: Methods using test sieves of woven wire cloth and perforated metal plate». 1988, 13.

45. Gulyaev I., Dolmatov A., Kharlamov M. et al. Arc-plasma wire spraying: an optical study of process phenomenology. Journal of Thermal Spray Technology. 2015. (24), 1566-1573. https://doi.org/10.1007/s11666-015-0356-6

46. Fialko N., Dinzhos R., Sherenkovskii J. et al. Influence on the thermophysical properties of nanocomposites of the duration of mixing of components in the polymer melt. Eastern-European Journal of Enterprise Technologies. 2022. 2(116), 25–30. https://doi.org/10.15587/1729-4061.2022.255830

47. Gu Y., Zhang W., Xu Y. et al. Stress-assisted corrosion behaviour of Hastelloy N in FLiNaK molten salt environment. npj Mater Degrad. 2022. (6), 90.

https://doi.org/10.1038/s41529-022-00300-x

48. Kvasnytskyi V., Korzhyk V., Kvasnytskyi V. et al. Designing brazing filler metal for heat-resistant alloys based on NI$_3$AL intermetallide. Eastern-European Journal of Enterprise Technologies. 2020. 6(108), 6–19. https://doi.org/10.15587/1729-4061.2020.217819

49. Han J., Shi Y., Zhang G. et al. Minimizing defects and controlling the morphology of laser welded aluminium alloys using power modulation-based laser beam oscillation. J. Manufacturing Processes. 2022. (83), 49–59. https://doi.org/10.1016/j.jmapro.2022.08.031

50. Skorokhod A., Sviridova I., Korzhik V. Structural and mechanical properties of polyethylene terephthalate coatings as affected by mechanical pretreatment of powder in the course of preparation. Mechanics of Composite Materials. 1994. 30(4), 455–463.

51. Kharlamov M., Krivtsun I, Korzhyk. V. Simulation of motion, heating and breakup of molten metal droplets in the plasma jet at plasma-arc spraying. Journal of Thermal Spray Technology. 2015. (24), 659–670. https://doi.org/10.1007/s11666-015-0216-4

52. Bobzina K., Ernsta F., Richardta K. et al. Thermal spraying of cylinder bores with the plasma transferred wire arc process. Surface and Coatings Technology. 2008. 202(18), 4438–4443. https://doi.org/10.1016/j.surfcoat.2008.04.023

53. Fan H., Kovacevic R. A unified model of transport phenomena in gas metal arc welding including electrode, arc plasma and molten pool. J. Phys. D: Appl. Phys. 2004. (37), 2531–2544. https://doi.org/10.1088/0022-3727/37/18/009

54. Haidar J., Lowke J. Predictions of metal droplet formation in arc welding. J. Phys. D: Appl. Phys. 1996. (29), 2951–2960. https://doi.org/10.1088/0022-3727/29/12/003

55. Nemchinsky V. Size and shape of the liquid droplet at the molten tip of an arc electrode. J. Phys. D: Appl. Phys. 1994. (27), 1433–1442. https://doi.org/10.1088/0022-3727/27/7/014

56. Kelkar M., Heberlein J. Wire-arc spray modeling. plasma chemistry and plasma processing. 2002. (22), 1–25. https://doi.org/10.1023/A:1012924714157

57. Bolot R., Planche M., Liao H. et al. A three-dimensional model of the wire-arc spray process and its experimental validation. J. Mater. Process. Technol. 2008. (200), 94–105. https://doi.org/10.1016/j.jmatprotec.2007.08.032

58. Chon Y., Liang X., Wei S. et al. Numerical simulation of the twin-wire arc spraying process: Modelling the high-velocity gas flow field distribution and droplets transport. Journal of Thermal Spray Technology. 2012. 21(2), 263–274. https://doi.org/10.1007/s11666-011-9723-0

59. Eggers J., Dupont T. Drop formation in a one-dimensional approximation of the navier-stokes equation. J. Fluid Mech. 1994. (262), 205-221. https://doi.org/10.1017/S0022112094000480

60. Hussary N., Heberlein J. Atomization and particle-jet interactions in the wire-arc spraying process. Journal of Thermal Spray Technology. 2001. 10(4), 604–610. https://doi.org/10.1361/105996301770349123

61. Pourmousa A., Mostaghimi J., Abedini A. et al. Particle size distribution in a wire-arc spraying system. Journal of Thermal Spray Technology. 2005. 14(4), 502–510. https://doi.org/10.1361/105996305X76522

62. Gedzevicius I., Valiulis A. Analysis of wire arc spraying process variables on coatings properties. J. Mater. Process. Technol. 2006. (175), 206–211. https://doi.org/10.1016/j.jmatprotec.2005.04.019

63. Hussary N., Heberlein J. Effect of system parameters on metal breakup and particle formation in the wire arc spray process. Journal of Thermal Spray Technology. 2007. 16(1), 140–152. https://doi.org/10.1007/s11666-006-9006-3

64. Fialko N., Prokopov V., Meranova, N. et al. Thermal physics of gasothermal coatings formation processes. State of investigations. Fizika i Khimiya Obrabotki Materialov. 1993. (4), 83–93.

65. Skorokhod, A., Sviridova, I., Korzhik, V. The effect of mechanical pretreatment of polyethylene terephthalate powder on the structural and mechanical properties of coatings made from it. Mechanics of Composite Materials. 1995. 30(4), 328–334. https://doi.org/10.1007/BF0063475

66. Fialko N., Dinzhos R., Sherenkovskii J. et al. Establishing patterns in the effect of temperature regime when manufacturing nanocomposites on their heat-conducting properties. Eastern-European Journal of Enterprise Technologies. 2021. 4(112), 21–26. https://doi.org/10.15587/1729-4061.2021.236915

67. Tillmann W., Abdulgader M. Wire composition: Its effect on metal disintegration and particle formation in twin-wire arc-spraying process. Journal of Thermal Spray Technology. 22(2–3), 352–362. https://doi.org/10.1007/s11666-012-9870-y

68. Wang P., Li X., Zhou X. et al. Numerical simulation on metallic droplet deformation and breakup concerning particle morphology and hollow particle formation during gas atomization. transactions of nonferrous metals society of China. 2024. 7(34), 2074 2094. https://doi.org/10.1016/S1003-6326(24)66526-X

69. Ibrahim M., Gobber F., Hulme C. et al. Influence of atomizing gas pressure on microstructure and properties of nickel silicide intended for additive manufacturing. Metals. 2024. (14), 930. https://doi.org/10.3390/met14080930